



Continuous debonding monitoring of a patch repaired helicopter stabilizer: Damage assessment and analysis



S. Pavlopoulou^{a,*}, S.A. Grammatikos^b, E.Z. Kordatos^c, K. Worden^d, A.S. Paipetis^e, T.E. Matikas^e, C. Soutis^a

^a University of Manchester, Composites Centre, School of Materials, Manchester, UK

^b Department of Architecture and Civil Engineering, University of Bath, Bath, UK

^c Materials and Engineering Research Institute, Sheffield Hallam University, Sheffield, UK

^d Department of Mechanical Engineering, University of Sheffield, Sheffield, UK

^e Department of Materials Engineering, University of Ioannina, Ioannina, Greece

ARTICLE INFO

Article history:

Available online 16 March 2015

Keywords:

Lamb waves

Lock-in thermography

Principal component analysis

Outlier analysis

ABSTRACT

The present work focuses on the structural health monitoring of an aluminium vertical helicopter stabiliser with a pre-introduced crack which was repaired with an adhesively bonded composite patch. The structure was monitored under bending fatigue and its performance was evaluated with Lamb waves, lock-in thermography and ultrasonic testing. Outlier analysis of Lamb waves captured the onset and progress of the damage in the form of patch debonding, enabling the identification of five damage-severity regions. Principal component analysis showed distinctive clusters that corresponded to different damage levels while the application of principal curves on the selected features proved to be an additional damage detection index. Amplitude and phase lock-in images accurately captured the onset and evolution of the damage in the form of patch debonding and honeycomb/skin debonding in agreement with the damage indices obtained from Lamb waves. C-scan further validated the damage mechanisms that were captured by the other methods.

© 2015 Elsevier Ltd. All rights reserved.

1. Background

This work focuses on adhesively bonded composite patches as a repair technique. This technology was first introduced to Australian military aircraft industry in the early 1970s and later in the USA in the early 1980s [1] in an attempt to prolong the life of ageing aircraft and to address the repair challenges in the new composite ones in a cost effective and reliable way. The considerable performance of the technique extended its application to civil aviation [2].

External patch repair is a type of repair that aims to provide a temporary restoration of the mechanical strength at regions that are not so critical in terms of structural performance [3]. There are certain design parameters which need to be considered before the application of an external patch such as the patch thickness, the overlap length, the adhesive thickness and the design scenario. A complete review was made by Hart-Smith, based on the results of a theoretical model [4,5] and further developed by Hu and Soutis [6]. An evaluation on the benefits of the use of one-sided and two-sided external patches can be found in previous work

[7]. Studies have shown that adhesively bonded repairs can restore up to 80% of the original structural strength [8].

In recent years, researchers have become increasingly interested in the problems related to repair patches that can emerge either from design issues or from extensive loading, such as the risk of debonding between the patch and the substrate when the ultimate shear strength of the adhesive is exceeded [9]. A number of studies have investigated these phenomena [10–12]. Clearly, a reliable in service monitoring of the performance is a very critical step towards the certification of the technique by the Civil Aviation Authorities, especially of primary load carrying structures [2,13].

A number of non destructive techniques have been used in order to assess performance of external bonded repairs in an off-line and on-line mode. Among the most notable work that can be found in the literature are; infrared thermography (IRT) has been effectively used for the off-line monitoring of artificially introduced delamination of CFRP patches from their aluminium substrate and for the on-line monitoring under fatigue loading [14]. Digital Image Correlation (DIC) has been used for the reliable on-line assessment of external and scarf repairs under tensile loading [15]. Despite the accuracy and reliability of the aforementioned techniques, they usually require a priori knowledge of the presence of damage and its location, and they require the use of expensive

* Corresponding author. Tel.: +44 (0)7826469399.

E-mail address: sofia.pavlopoulou@manchester.ac.uk (S. Pavlopoulou).

and bulky equipment with any problem arising due to accessibility restriction or they require the removal of parts. These can lead to an increased inspection cost that might require downtime of the aircraft. Therefore the next step in damage detection moves towards structural health monitoring techniques [16].

Structural health monitoring employs built-in structural diagnosis methods which utilise a number of on-line monitoring methods where a number of sensors (sensor arrays or optic fibres) can be inserted in the critical plies of the patch. These can continuously monitor the structural integrity. The aforementioned concept is a relatively new concept which needs to be extensively investigated with the aim of industrial approval. Among the most notable work that can be found; an optical fibre sensor array was used for the monitoring of the crack and delamination growth under a bonded repair [17]; a SMART layer employing Lamb waves was used in order to evaluate the cure and bond level of a composite repaired panel along with damage under fatigue loading [18].

The current work focuses on the monitoring of a repaired helicopter stabilizer subject to bending fatigue, with Lamb waves, lock-in thermography and ultrasonic inspection (C-scan). In Section 2, a brief background is presented related to the use of Lamb waves for damage detection focusing on the signal post processing through outlier analysis and linear and nonlinear principal component analysis. In the same section a brief background of the lock-in thermography is presented. In Section 3 the experimental set up is illustrated and in Section 4 the results for the three monitoring techniques are presented and discussed in detail. Finally, in Section 5, the most important conclusions of the work are discussed.

2. Structural health monitoring techniques

2.1. Lamb waves

Lamb waves are elastic perturbations that propagate in plate-like structures. They are a type of ultrasonic waves that are guided between parallel free surfaces, such as the upper and lower surfaces of a plate. Lamb waves exist in two possible modes, the symmetric modes and the anti-symmetric modes, which represent the motion of the particles in a longitudinal and in a parallel to the propagation direction respectively. For more information the reader is referred to the literature reviews [19,20]. A considerable number of researchers have used several approaches for the effective use of Lamb waves for damage detection purposes, such as modelling and numerical analysis [12], physics-based [21] and signal processing-based [22] techniques. Among the most notable works performed on composite repaired structures; the first anti-symmetric Lamb wave mode was generated at low frequencies in sandwiches and composite single and double-lap repairs in order to detect impact damage [23]. Moreover two SMART layers with an embedded network of piezoelectric actuators/sensors were inserted into a boron/epoxy laminated patch at different ply-locations to successfully monitor crack growth via Lamb wave excitation [24]. However very limited work has been performed on large scale, industry representative structures in order to demonstrate the efficiency of the monitoring techniques under in-service operating conditions.

2.1.1. Outlier analysis

Outlier analysis (OA) is referred to as the process of statistical determination of the class of a set of data, dealing with two general classes: normal or damaged. The aim is the detection of outliers within a set of given data. These outliers reflect the value that makes the monitored system deviate from the normal condition, corresponding to a damaged condition. The deviation is estimated

on the basis that the normal condition data follow a Gaussian distribution.

The discordancy value in the case of multivariate data is called the *Mahalanobis squared-distance* and it can be estimated by the following equation:

$$D_{\zeta} = (\underline{x}_{\zeta} - \bar{\underline{x}})^T S^{-1} (\underline{x}_{\zeta} - \bar{\underline{x}}) \quad (1)$$

where, \underline{x}_{ζ} is the potential outlier feature vector and $\bar{\underline{x}}$ and S are the mean vector of the normal condition features and the corresponding sample covariance matrix, respectively. T indicates transpose. The estimation of an assigned threshold, is performed through the employment of a Monte Carlo approach and by taking into consideration the dimensions of the extracted features for the monitored system. Any observation that lies above the threshold is classified as an outlier; further details on the analysis and relevant applications can be found in earlier works [22,25–27].

2.1.2. Linear and nonlinear principal component analysis

Linear principal component analysis (PCA) has been used for the representation of multivariate sets of data in a reduced-dimensional space to enable an easier data interpretation. This is achieved through the projection of the data into a lower-dimensional space (e.g. a new set of axes) through orthogonal linear transformations. Each of these new variables is a linear combination of the original variables. In the current work PCA was performed through the application of the singular value decomposition (SVD). Notable work that employed PCA for damage detection purposes can be found in the literature [27–29].

Principal component analysis projects the data on principal components by extracting linear relationships (e.g. by projecting data into lines). In the current work a more generalised concept was established which allows the projection of the data into curves or surfaces instead of lines or planes, namely the nonlinear principal component analysis (NLPCA). This is achieved through the extraction of both linear and nonlinear relationships such as higher-order statistics, through the minimisation of orthogonal projection lengths from the data points to the curve. This is graphically shown in Fig. 1. NLPCA can be a valuable tool for the interpretation of high-dimensional data sets in structural health monitoring problems. However, until now, it has not been systematically exploited for structural health monitoring applications and only a few case studies can be found in the literature [30,31]. A FORTRAN programme was used for the implementation of the current work which starts with a prior line, the first principal component [27,31,32] and after a number of iterations bends to fit the distribution of the processed data. The hypothesis is that the arc length of the principal curve could serve as a valuable damage index which could describe the deviation of the system from the baseline reference with a single line.

2.2. Lock-in thermography

Lock-in thermography (LT) is an active thermographic technique usually employed to identify internal imperfections in materials or follow any degradation process during service. The advantage of LT over other methods is the synchronisation of the thermal sensor with the thermal stimulation source. Ultrasonics, electrical current, optical (lamps) or mechanical loading [14] are the most common thermal excitation techniques. In the case of mechanically loaded structures, LT is applied on-line in order to follow the structural deterioration process. Mechanical loading generates inherent mechanical stresses which through thermomechanical coupling are detectable by the thermal camera. Recorded mechanical stresses stem from the presence of stress raisers i.e.

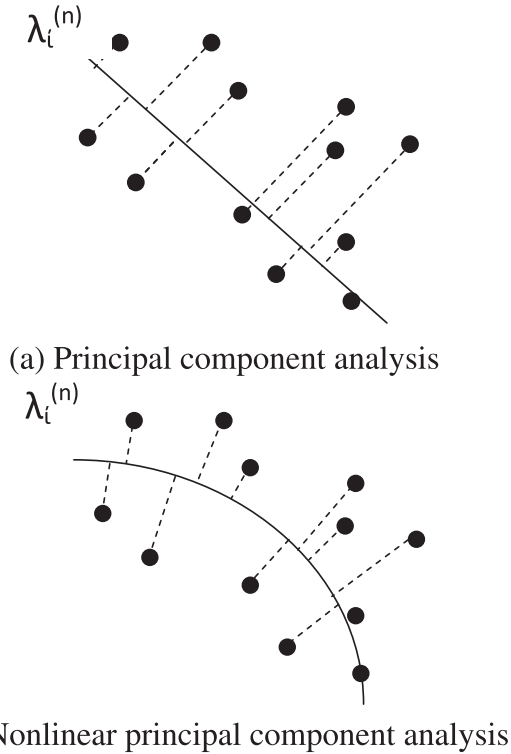


Fig. 1. (a) Schematic illustration of the data projection nature for the linear and (b) nonlinear principal component analysis (arc length λ).

cracks, defects. Therefore, stress raisers are the cause of damage initiation in a structure and its subsequent final failure [33].

When a structure is subjected to a mechanical stress field, both thermoelastic and thermoplastic couplings occur. Thermoelastic coupling does not induce any change in the structure mean temperature as it takes place when it is mechanically loaded in the elastic region during fatigue. On the other hand, thermoplastic coupling phenomena occur when the structure is loaded beyond the elastic region. These lead to internal friction, plastic deformation and subsequent heat dissipation which can be captured using a thermal sensor/system.

Assuming reversible adiabatic elastic conditions for a thermally isotropic solid [34], the well-known thermoelastic effect, may be described as shown in Eq. (2):

$$\Delta T = (-\alpha/\rho C_p) T \Delta \sigma = K_m T \Delta \sigma \quad (2)$$

where ρ is the mass density, C_p the specific heat and constant pressure, α the Coefficient of Thermal Expansion (CTE), T the absolute temperature, ΔT the change in temperature in Kelvin degrees, K_m the thermoelastic coefficient and $\Delta \sigma$ represents the change in the sum of principal stresses. Carbon fibres are thermally anisotropic, as they possess a negative CTE in the longitudinal direction and a positive CTE in the transverse direction [35,36]. Wong [37] reported positive CTE values at the two principal directions, albeit with different values.

Based on the fact that the signal is linearly recorded by a thermal sensor [38] and assuming that all other parameters are constant (for small temperature changes K_m is constant), the relative stress difference induced thermoelastically, is directly related to the relative temperature difference both for the local stress difference and temperature difference σ and T , respectively and the stress difference and temperature difference away from a cracked/defected area $\Delta \sigma_\infty$ and ΔT_∞ , respectively. Therefore, Eq. (2) can lead to:

$$\Delta \sigma / \Delta \sigma_\infty = \Delta T / \Delta T_\infty \quad (3)$$

In other words, the recorded normalised amplitude gradient on the specimen surface is equal to the normalised stress gradient. In this way, all amplitude images may be transformed to stress concentration (SC) maps simply by normalising the local amplitude values by the amplitude value away from the induced stress concentration, or the far field amplitude value. In general, high amplitude areas could be attributed both to stress concentrations due to thermoelastic effects and temperature gradients induced by localised damage [33].

3. Experimental set up

3.1. Design and damage evaluation of a repaired helicopter vertical stabilizer

A vertical stabilizer of a helicopter located on the tail boom and manufactured by PZL-Swidnik/AgustaWestland (Poland) was selected as a representative aeronautical structure for repair and non-destructive testing. The panel was of a honeycomb construction, the core of which was made of HexWeb CRIII-5/32-5052-.001N-3.8 and the skin of AL-2024 T3 alloy sheet, of a thickness variation from 0.6 mm to 1.5 mm. Prior to the selection of the area to be repaired, bending fatigue was performed and the most critical region was identified to be around the rivets/bolted joints at the centre of the stabilizer as illustrated in Fig. 2(a). An artificially 35 mm crack that would be repaired by a bonded composite patch was introduced, located close to the hole as shown in Fig. 2(b) and (c).

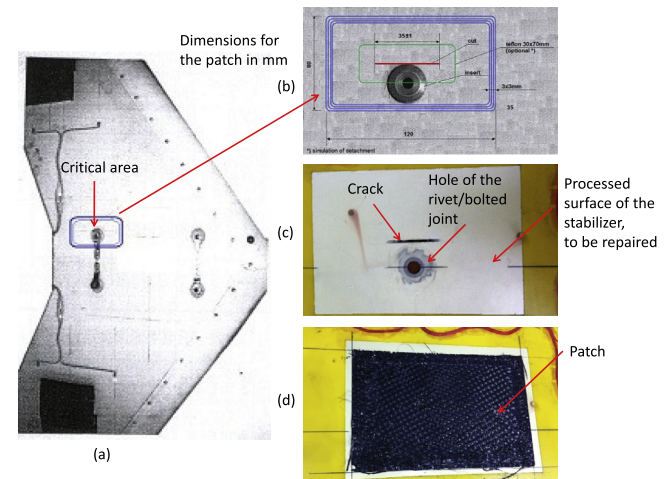


Fig. 2. (a) Critical area and proposed location (blue line) for the attachment of the repair patch (b) schematic illustration of the repaired region (c) image of the processed surface of the stabilizer around the crack and the hole before the attachment of the patch (d) final implementation of the patch.¹ (For interpretation of the references to colour in this figure legend, the reader is referred to the web version of this article.)

Table 1

Stepping configuration scenario for the patch (total thickness = 1.16 mm).

| Number of layers | Direction | Dimensions (mm) |
|------------------|-----------|-----------------|
| L1 | 90° | 80 × 120 |
| L2 | 0° | 74 × 114 |
| L3 | 90° | 68 × 108 |
| L4 | 0° | 62 × 102 |

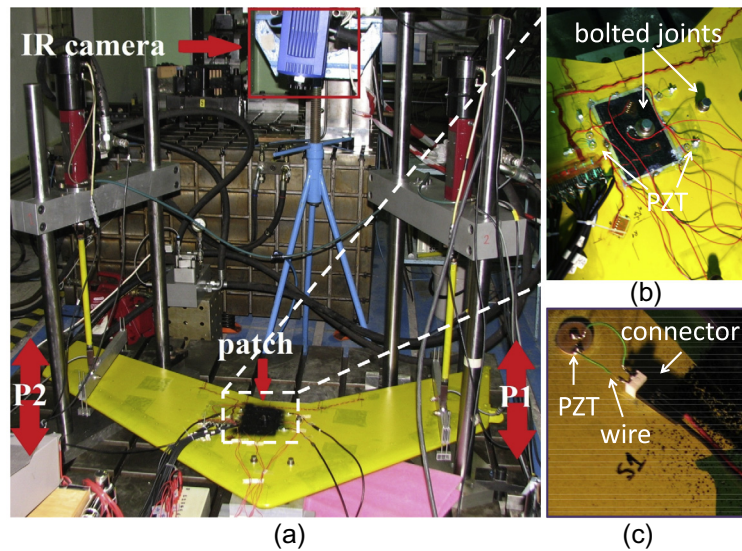


Fig. 3. (a) Schematic illustration of the repaired stabilizer (a) test set up for bending fatigue of the repaired stabilizer at two loading points P1 and P2 with the IR camera positioned on top of the repaired region (b) repair patch sprayed with a black paint for thermography inspection; one repaired and one non repaired bolted joint and (c) PZT transducer for Lamb wave monitoring.¹

The repair patch consisted of 4 plies AGP 280 (Hexcel 43280S) with a stacking ply sequence $[90/0]_2$ and total thickness equal to 1.16 mm. First the repaired surface was prepared using BR127 primer, Fig. 2(c), and each ply was impregnated with carbon nanotube (CNT) doped epocast. Each ply was cut to the final dimensions and laid up on the repaired region following a stepwise configuration as outlined in Table 1. Finally, a heating blanket was used for 2 h at 93 °C under vacuum conditions for the curing. The final cured patch is shown in Fig. 2(d). A C-scan was performed on the demonstrator prior to testing for evaluation of the bonding quality of the composite patch as shown in Fig. 19(a).

The testing scenario selected was representative of the kind of loading such structures are subject to, namely bending fatigue. As illustrated in Fig. 3(a), there are two loading points (P1 and P2). The load was distributed between the two points so that the moment about the fixed (repaired region) area, was equal both at the right and left side. The distance between the centre of the repaired region and the two loading points P1 and P2 was 580 and 520 mm, respectively. The structure after the application of the repair consisted of two bolted joints, one repaired and one non repaired as it is displayed in Fig. 3(b) which proved to be critical in the analysis of the lock-in thermography images. The fatigue history is illustrated in Fig. 4. All tests were performed at a frequency equal to 20 Hz.

3.2. Monitoring with Lamb waves

Four piezoelectric transducers (diameter = 10 mm, thickness = 1 mm) were used for the monitoring with Lamb waves supplied by CeramTec, Germany. The substrate surface was processed with a sandpaper in order to obtain a rough surface which would ensure a good adhesion of the sensors to the surface, Fig. 3(b) and (c). Two of the PZTs (A1, A2) operated as actuators, exciting the tested demonstrator and the other two (S1, S2) operated as sensors receiving the output response, forming two propagation paths, path 1 and path 2 (Fig. 5). This means that when actuator A1 was exciting the demonstrator only sensor S1 was recording

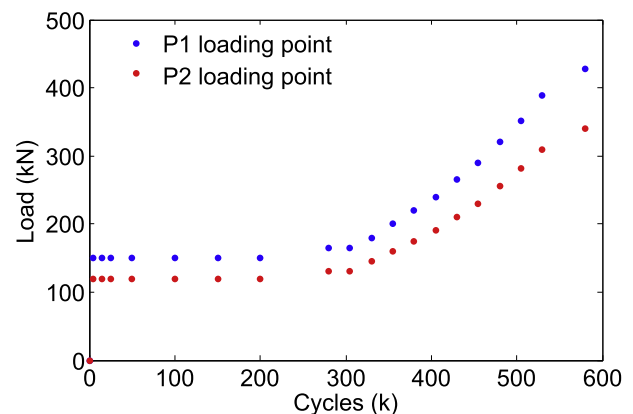


Fig. 4. Load history of the helicopter stabilizer, subjected to bending fatigue, $f = 2$ Hz; P1 and P2 correspond to applied load points of Fig. 3(a).

the obtained signals, and when actuator A2 was exciting the demonstrator, only sensor S2 was recording the resulting signals.

The location of the employed transducers was selected in such a way that the stronger incident output signal would directly interact with the most interesting regions where damage was expected to develop, perpendicular to the crack orientation. These were the edges of the patch and the crack of the stabilizer. In addition, their placement was intended to be as close to the patch as possible in order to minimise reflection of the propagating wave from other structural features and not to interfere with the image recording by thermography, Fig. 5.

The excitation signal was a 10-Volt peak-to-peak amplitude, 5-cycle sine pulse modulated by a Hanning window and the excitation frequency was 200 kHz. The wave generator that was used was a TTi TGA 1230 30 MHz model and the data acquisition was performed with a HAMEG HMO 2022 digital oscilloscope at sampling frequency equal to 25 MHz. For each set of signals, 512 averages were captured in order to minimise the effect of noise. The excitation signal as shown in Fig. 6(a) was modulated by a Hanning window in order to maximise the energy that would be 'guided' to the tested demonstrator. This can be verified by the Fourier spectrum of the time signal in Fig. 6(b).

¹ The contained data are property of PZL-Swidnik S.A. and any further reprinting and usage cannot be made without PZL-Swidnik S.A. written permission.

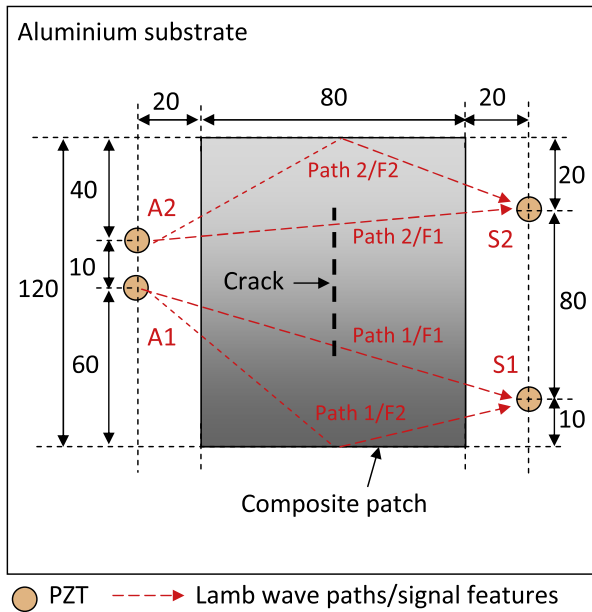


Fig. 5. Schematic illustration of the PZTs arrangement where A = actuator and S = sensor; dimensions in mm.

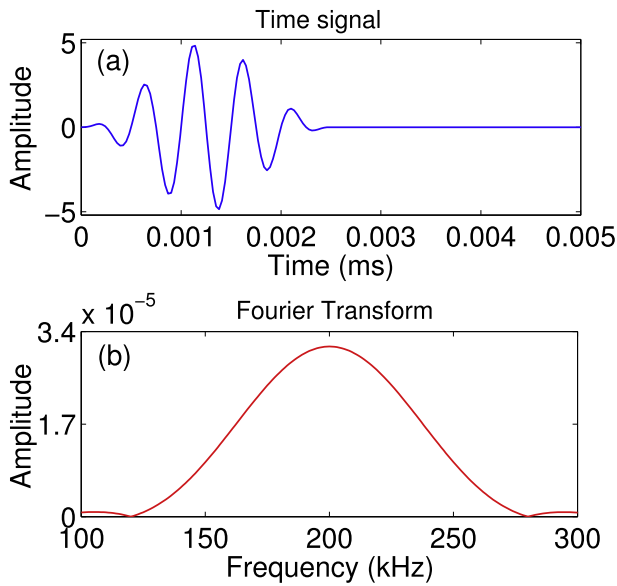


Fig. 6. (a) Excitation signal at 200 kHz and (b) its Fourier spectrum.

As part of the post-processing of the recorded waveforms, appropriate signal features had to be selected in order to reduce the dimensions of the data sets while isolating the regions of interest. Fig. 7 illustrates the resulting waveforms for the baseline reference set, meaning the response prior to any loading, which is used in order to represent the undamaged, 'healthy', condition. In the same figure, the selected features are illustrated for both paths 1 and 2. Two features were selected for each waveform, the first (F1) corresponding to the incident wave which directly propagates through the bonded area and the edge of the crack and the second (F2) corresponding to the first reflection occurring from the edges of the patch and the crack. The rest of the captured waveform exhibits extensive attenuation as the waves undergo multiple reflections at the boundaries of the different features. The selected features for each propagation path can also be schematically seen in Fig. 5.

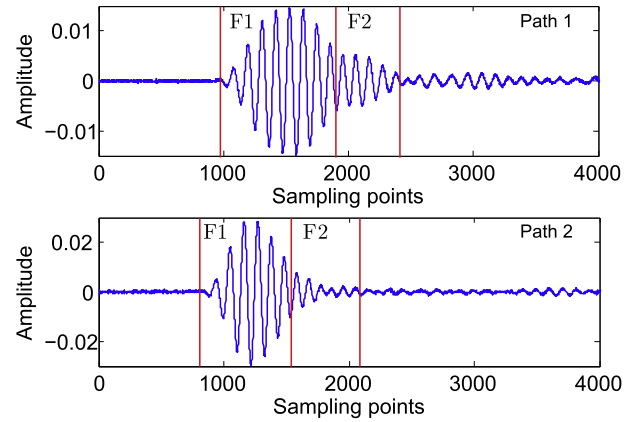


Fig. 7. Response for the baseline reference state - 'healthy' condition along with the selected features for paths 1 and 2. Feature 1 (F1) represents the incident wave, while Feature 2 (F2) corresponds to the first deflection occurring from the patch and crack (also illustrated in Fig. 5).

3.3. Monitoring with lock-in thermography

For the acquisition of the thermal dynamic response, the Jade 510-CEDIP-MIR infrared camera was employed, as shown in Fig. 3(a). It employs a cooled indium antimonide (InSb) detector (3–5 μm), with a frame rate ranging from 50 to 150 Hz and focal plane array (FPA) pixel format of 320 (H) \times 240 (V).

The thermal camera was appropriately positioned vertically facing the top (repaired) surface of the stabilizer (Fig. 3(a)); the patched area was painted with a black matt paint. This renders the emissivity of the inspected surface close to that of a black body ($\epsilon = 1$). The distance between the camera and the stabilizer was approximately 0.8 m. Lock-in of the camera acquisition was performed utilising the electrical waveform employed for the P1 loading moment (Figs. 3(a) and 4). The synchronisation of the frequency of the thermal sensor and the testing machine enabled amplitude and phase images. The frame rate of the infrared camera was set to 25 Hz.

After 580 k fatigue cycles, at the end of the test, a clear debonding could be visually observed as illustrated in Fig. 8 which signified the end of the mechanical testing. Thermographic images were captured at different number of applied fatigue cycles and discussed in following sessions.

4. Results and discussion

4.1. Lamb waves-outlier analysis and principal component analysis

In order to build the appropriate matrices for the subsequent analysis, 100 signals were recorded for the baseline reference set (0 cycles – Test sets 1–10, Table 2) and 10 signals were recorded for each subsequent damage set; each copy of the recorded signal is here referred to as "observation". These signals were recorded in an off-line mode, which means that test was stopped for the recording of the signals. As explained and shown in previous work [25], this would ensure a sufficient set of data for the accurate training and application of outlier analysis and PCA algorithms. Furthermore the selected features (F1 and F2 as shown in Fig. 7), were further subsampled (the sampling points were reduced to 50 following a fixed step) in order to reduce the dimensions of the data. As has been previously proven it does not affect the resolution of the method [26]. The sampling points number of the reduced dimensional features are here referred to as "dimensions".

After the pre-processing of the obtained signals, OA and PCA were performed in a comparative way in order to identify the

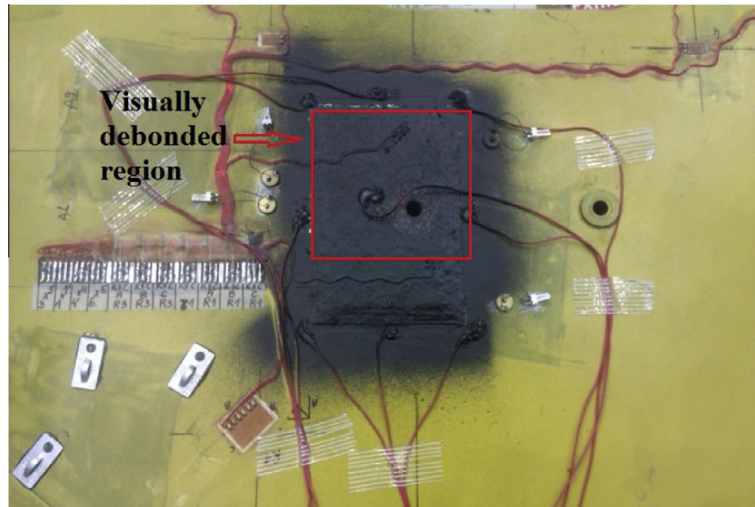


Fig. 8. Final debonding after 580,000 cycles of bending fatigue testing.

Table 2

Test sets of the outlier analysis and fatigue cycles.

| | | | | | | | | | | | |
|-----------|---------|---------|---------|---------|---------|---------|---------|---------|---------|---------|---------|
| Test sets | 1–10 | 11–20 | 21–30 | 31–40 | 41–60 | 61–70 | 71–80 | 81–90 | 91–100 | 101–100 | 111–120 |
| Cycles | 0 | 500 | 5 k | 15 k | 25 k | 50 k | 100 k | 150 k | 200 k | 280 k | 305 k |
| Test sets | 121–130 | 131–140 | 141–150 | 151–160 | 161–170 | 171–180 | 181–200 | 201–210 | 211–220 | 221–230 | |
| Cycles | 330 k | 355 k | 380 k | 405 k | 430 k | 455 k | 480 k | 505 k | 530 k | 580 k | |

agreement between the two methods and in order to explain the behaviour of the OA classes based on the orientation of the respective clusters in a 2-dimensional subspace. The aim of the analysis was the classification of the recorded waveforms and the estimation of their deviation from the baseline reference set. Based on the amount of deviation, appropriate assumptions were made for the presence of damage in the tested structure.

For the illustration of the PCA results, only the first two principal components were considered, since they accounted for the highest percentage of variance. For the purpose of the outlier analysis, the 1% exclusive threshold value for novelty for a 100-observation, 50-dimensional problem was estimated after 1000 trials which was found to be approximately the same for all paths, namely 100. This threshold (estimated through the Monte Carlo approach) is here denoted as Threshold 1. From the baseline reference data set, 90 observations were used as a training set in order to train the algorithm, and the remaining 10 observations were used as a validation set in order to evaluate how effectively the algorithm can identify the normal condition, as was performed for PCA. Table 2 illustrates the test sets of the outlier analysis and the respective fatigue cycles. As should be noted, the sets of data were recorded without any loading and compared to the last recorded set when the test continued the next day. In this case a baseline reference set was captured prior to testing in order to ensure that the system was not affected by any possible temperature variations, noise or other parameters. No effect was noticed due to the aforementioned causes.

Figs. 9 and 10 illustrate the OA results and the PCA results for the selected features for propagation path 1. All the OA figures have the same scale in the y-axis for comparison purposes. Five areas can be distinguished in Figs. 9(a) and 10(a) based on the level of deviation from the assigned threshold (threshold 1), noted in the figure as R1–R5, each region corresponding to a different colour. The same colours have been assigned to the corresponding clusters in the PCA figures in Figs. 9(b) and 10(b). Regions R1 and R2 (from 0

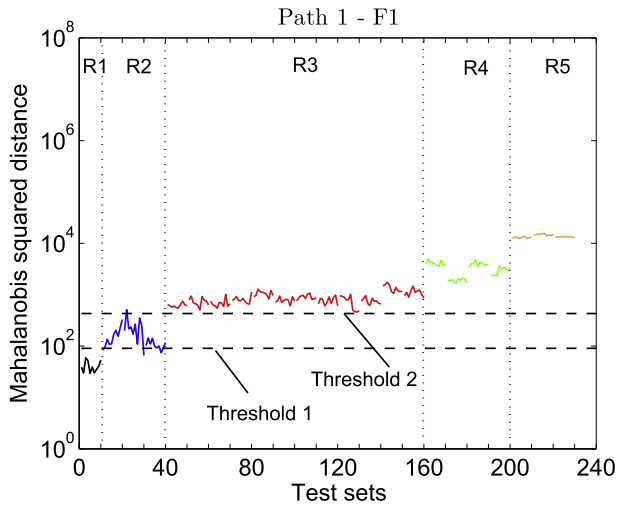
to 15,000 cycles) are for both features very close to the threshold, while the deviation from the normal condition is not significant. However, region R2 is flagged as outlier (e.g. above the threshold). At this stage, the stabilizer was loaded for just 15,000 cycles at low loads (120 kN at loading point P2 and 150 kN at loading point P1). Given the testing conditions and the little deviation of the region from the threshold, it was assumed that no critical damage could have occurred at this stage. Nevertheless, something in the structure changed, leading to the change of the boundary conditions. An assumption of the possible reason for this behaviour is the increase in the temperature of the stabilizer after a few loading cycles, or micro-cracks at the adhesive of the transducers as soon as the testing started. These small changes could be sufficient for the observed behaviour, without necessarily notifying about a critical damage. Therefore a second threshold was defined (threshold 2) as shown in Fig. 9(a).

For the estimation of this threshold, the data set of region R2 was divided in two subsets, in the following way; Subset 1: 11–25 test sets, Subset 2: 26–40 test sets. Then the maximum value of the estimated Mahalanobis squared-distance was denoted as the threshold value for each subset. Then the final threshold 2 was estimated by taking the mean of the two aforementioned values:

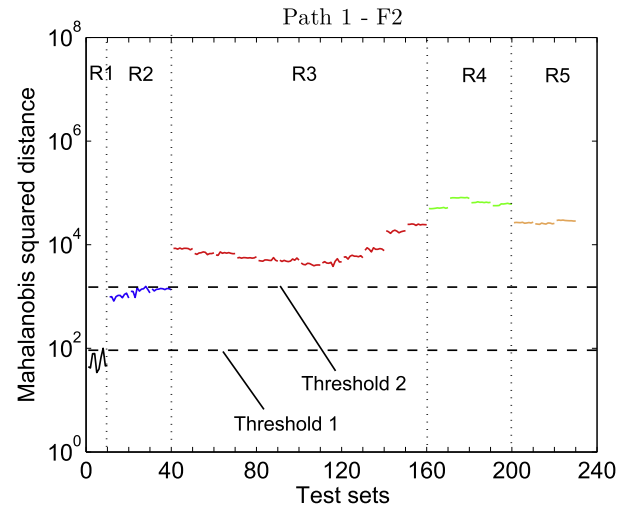
$$\text{Threshold 2} = \frac{\max(\text{MSD}_{\text{Subset 2}}) + \max(\text{MSD}_{\text{Subset 1}})}{2} \quad (4)$$

where Subset 1 = 11–25 test sets and Subset 2 = 26–40 test sets and MSD is the Mahalanobis squared-distance. The test sets are summarised in Table 2.

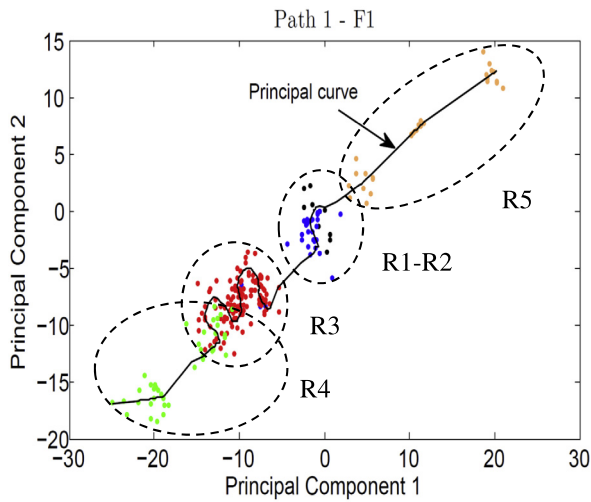
Threshold 2 could not be estimated through the Monte Carlo technique since the data sets that correspond to this stage no longer follow a Gaussian distribution. Both thresholds have been plotted at all subsequent figures, in an attempt to demonstrate the monitored system's behaviour in a more representative way. It is worth mentioning though that threshold 2 required a prior



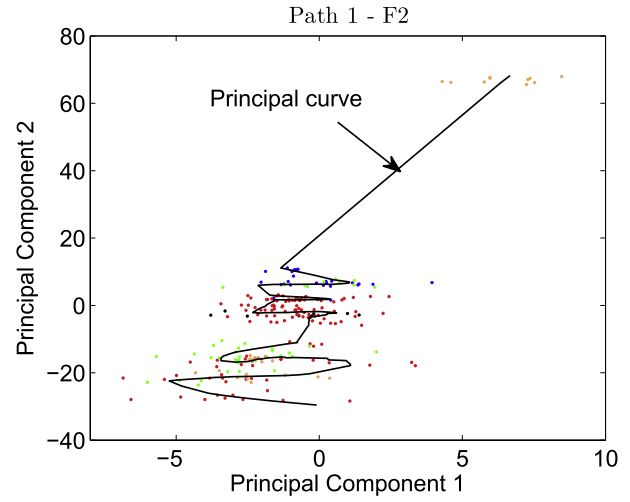
(a)



(a)



(b)



(b)

Fig. 9. (a) Outlier analysis (OA) and (b) principal component analysis (PCA) for path 1 – feature 1 (F1). Threshold 1 estimated through Monte Carlo technique and Threshold 2 assigned to reflect changes in boundary conditions, outliers above thresholds represent damage, regions R1–R5 show progressive damage increase in the form of increasing Mahalanobis distance OA values and as separate PCA clusters.

Fig. 10. (a) Outlier analysis (OA) and (b) principal component analysis (PCA) for path 1 – feature 2 (F2). Regions R1–R5 are only clear in OA results and not in PCA clusters. F2 exhibits higher OA values than F1 (R3).

knowledge of the system’s status, while threshold 1 was estimated without any prior knowledge of the system’s behaviour. This approach is a simple way to overcome what has been previously described. According to Tarassenko [39], in cases of on-line learning, it is important to enable the algorithm to adapt to novel data instead of simply converging to a stable model, in order to account for complex cases such as the one discussed here. This by itself is a case that needs to be further studied for future applications.

Region R3 (15,000– 405,000 cycles) in Fig. 9(a) is only slightly flagged above the thresholds but without any considerable deviation. However, there is a certain increasing tendency which suggests that damage has started accumulating in the monitored area (path 1). Region R4 (405,000–480,000 cycles) shows a higher deviation from the thresholds than region R3 while the region R5 (480,000–580,000 cycles) clearly corresponds to a stage where significant damage has developed. Feature 1 (F1), shown in Fig. 9(a), which corresponds to the part of the waveform that has been captured by the sensor without interacting with any other features/ boundaries, shows more distinctive differences than feature 2

(F2), shown in Fig. 10(a). However feature 2 (F2) exhibits higher values of deviation from the normal condition (higher Mahalanobis squared distance) (areas R3–R5).

Principal component analysis (PCA) results show how well the clusters that correspond to each region separate when they are projected on the baseline reference set (0 cycles – pristine condition). F1, shown in Fig. 9(b), exhibits a clear separation between the clusters, indicating the successful assignment of the regions in the OA, and verifying the deviation of the behaviour of the monitored system from the normal condition. As for feature (F2), which is shown in Fig. 10(b), even though there is a certain separation of the orange dots (R5) from the rest of the clusters, in general the technique does not provide the resolution of the OA.

Figs. 11 and 12 illustrate the same results but for path 2. The y-axis is scaled in the same way as for path 1 for comparison purposes. The first observation is that the same regions (R1–R5) can be assigned in the OA figures, which indicate the level of deviation from the baseline reference (pristine condition) and from the assigned thresholds as shown in Figs. 11(a) and 12(a). One difference is that region R4 starts one set of data later (e.g. 170 test sets) for the second feature (F2) compared to F1 for the same path and

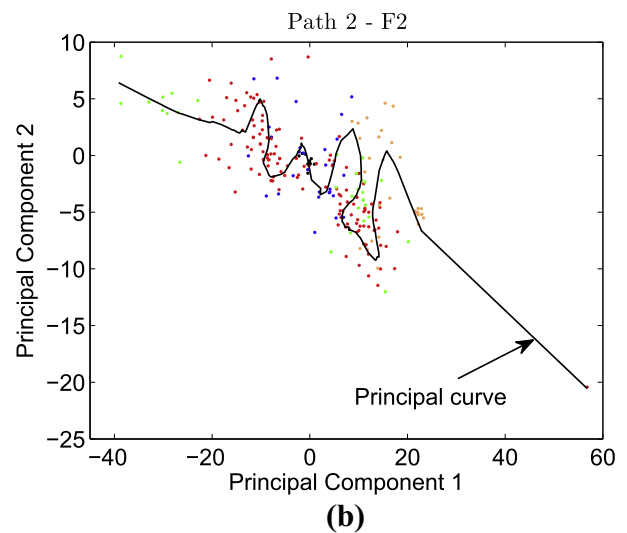
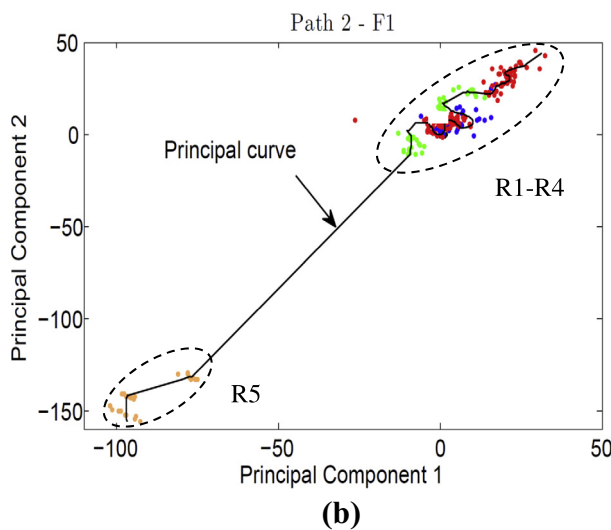
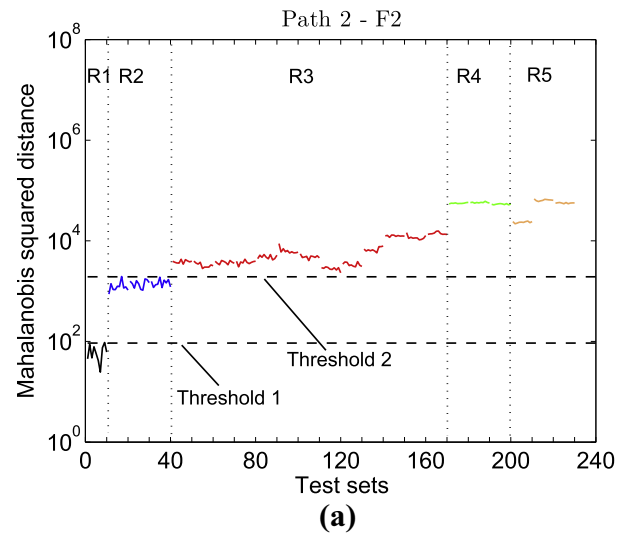
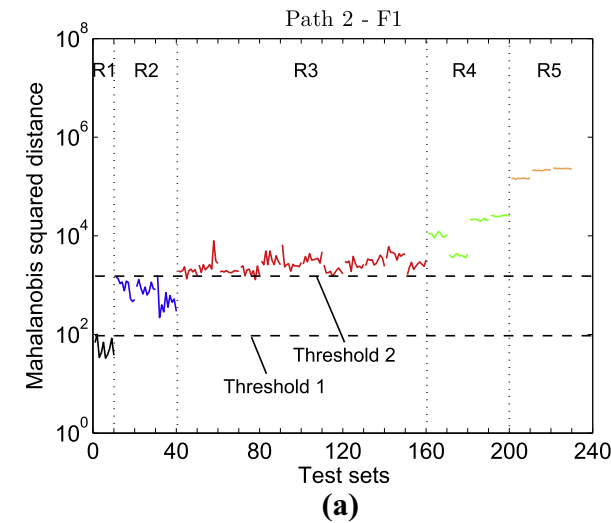


Fig. 11. (a) Outlier analysis (OA) and (b) principal component analysis (PCA) for path 2 – feature 1 (F1). Threshold 1 estimated through Monte Carlo technique and threshold 2 assigned to reflect changes in boundary conditions, outliers above thresholds represent damage, regions R1–R5 show progressive damage increase in the form of increasing Mahalanobis distance OA values and as separate PCA clusters (R1–R5).

Fig. 12. (a) Outlier analysis and (b) principal component analysis for path 2 – feature 2 (F2). Regions R1–R5 are clear in OA results and while PCA clusters can not be attributed to certain region.

also compared to both features F1 and F2 for path 1. Furthermore, PCA exhibits quite mixed clusters, from which only the region R5 can be separated for the F1, as shown in Figs. 11(b) and 12(b).

A comparison between the two paths shows that, their behaviour is in general similar. Region R3 is the one which mostly draws the attention, since it is the one which shows a certain deviation from the normal condition. The key requirement here is the identification of the damage sensitivity of each path with respect to an early stage damage onset detection, namely area R3. The OA for path 1 and path 2 exhibits similar results except for the second feature (F2), which shows significantly higher levels of deviation for path 1. In addition, PCA shows a more distinctive separation between the resulting clusters for the first feature (F1) of path 1 compared to the same feature for path 2. Even though this is not very clear at this stage, one could in general conclude that path 1 exhibits a relatively higher damage sensitivity, especially at the area where the first notable damage seems to develop, in region R3. This was later verified from the lock-in images which showed that the first noticeable type of damage was in the form of patch debonding which initiated at the repaired bolted joint. This

would significantly affect path 1 more than path 2 (Fig. 5), hence justifying the higher damage sensitivity as observed from OA and PCA results.

In addition, the proposed technique of the principal curves based on the NLPCA is performed here, the results of which can be found in the respective figure of the PCA results (Figs. 9–12). As illustrated, after 10 iterations, the principal curve fits very successfully the principal component clusters, starting from the first principal component and iteratively bending to match the required shape. The arc length of the curve is not plotted for this case study but it can be observed from the principal curves, that for all cases it would successfully describe the deviation of the clusters above 480,000 cycles from the rest which appear to be very close to each other. The same conclusion can not be derived for path 2 (F2, Fig. 12) where the clusters are quite mixed without a substantial separation.

4.2. Lamb waves – outlier analysis at the principal components

In the current section an alternative approach is attempted to assess the structural integrity of the tail stabilizer. This approach focuses on the OA of the principal components that are derived

from the principal component analysis. This means that the “observations”, original time signals, assigned for each feature in Section 4.1, would now be replaced with the principal components for each feature, as derived from the principal component analysis. The number of the selected principal components is selected based on the drop of variance. In this case, the first 10 principal components for all steps were considered to be adequate since they accounted for approximately 80% of the total variance of the set with some slight differences for each path/feature.

In the same way as with OA, the first 90 observations of the pristine condition were used as a training set while the rest were used for validation of the algorithm. The 1% exclusive threshold value for novelty for a 100-observation, 10-dimensional problem was estimated after 1000 trials which was found to be approximately the same for all paths (threshold 1). Threshold 2 was defined in a similar way as before.

Fig. 13 illustrates the variance drop that resulted from the linear PCA for propagation paths 1 and 2 and for both considered features. It was decided that the first 10 principal components accurately represent the higher percentage of the data variance. Therefore they were selected for the subsequent outlier analysis.

Feature 1 (F1) in Fig. 14(a) shows that the results are more representative of the assumption made for the OA on the original time signals in Section 4.1; it verifies that region R2 is not indicative of damage. This means that regions R1 and R2 are indeed labelled as inliers (below the threshold 1) while region R3 is very close to the threshold only slightly flagged above it without any considerable variation. In this case there was no need to assign threshold 2. It is only after 480,000 cycles that OA gives clear outliers (regions R4 and R5). On the other hand, feature 2 (F2) shown in Fig. 14(b) illustrates a slightly different behaviour, almost similar to the OA of the respective path/feature for the original time signals although the values of the deviation are smaller due to the change in the number of the dimensions of the feature (10-dimensional instead of 50-dimensional).

Fig. 15 illustrates the same OA results for propagation path 2. Feature 1 (F1) exhibits a similar behaviour for the same feature F1 of path 1, exhibiting lower deviation from the normal condition and the thresholds than what the respective original time signal showed in Section 4.1. In addition, regions R1 and R2 are below the threshold 1 and threshold 2, respectively, while region R3 is very close to threshold 2, exhibiting a relatively steady behaviour.

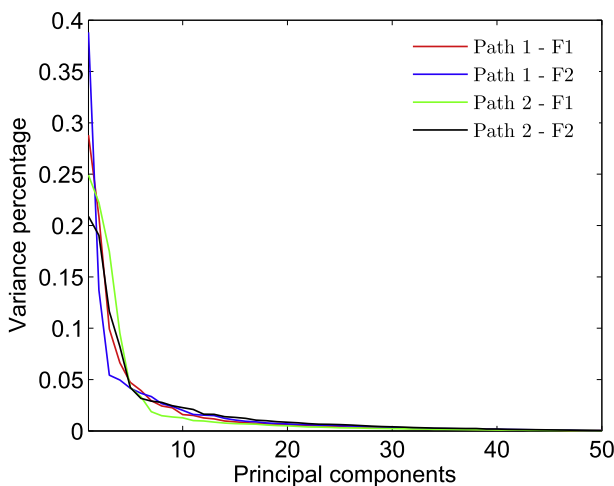


Fig. 13. Variance drop over the principal components for both propagation paths and selected features. First principal component accounts for the highest percentage of the total variance, the second principal component for the second highest percentage etc. The first 10 principal components account for 80% of the total variance of the set with only some slight differences for each path/feature.

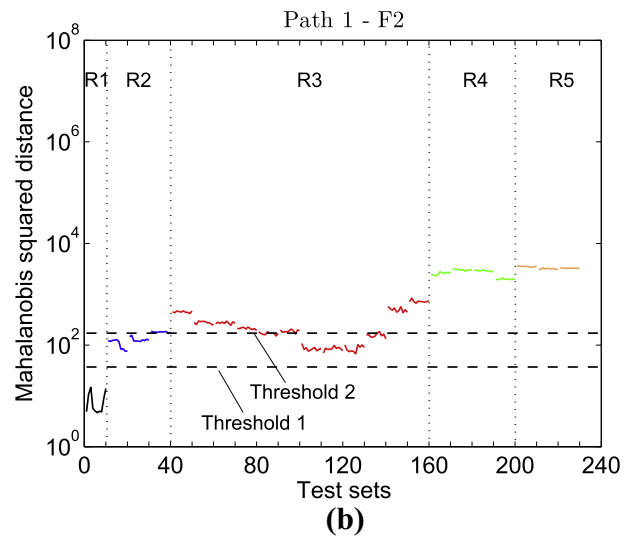
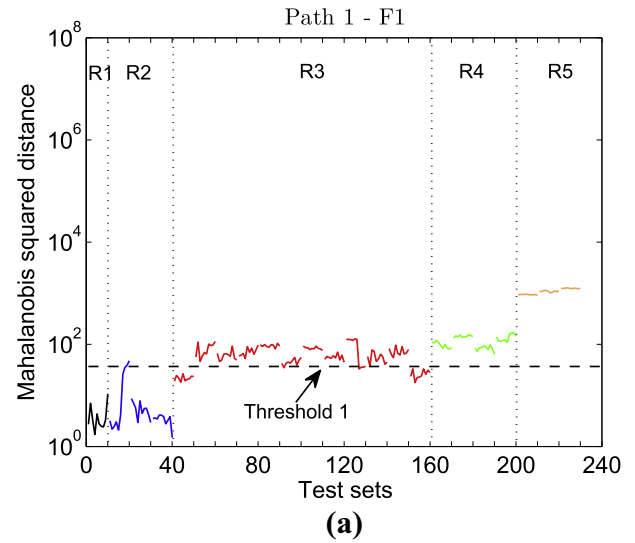


Fig. 14. (a) Outlier analysis at the first 10 principal components for path 1, corresponding to feature 1 (F1) and (b) feature 2 (F2).

In a similar way as with propagation path 1, R4 and R5 (above 480,000 cycles) are clearly flagged as outliers while the boundaries between the two regions are quite distinctive. On the other hand F2 exhibits a similar behaviour with the feature taken from the original time signal, without any underlying difference. The main assumption derived here is that at least F1 for both paths shows an improved behaviour and represents in a more reasonable way the structural integrity of the stabilizer. This is attributed to the fact that among the whole tested data set, only the main principal components were taken into consideration, which account for the highest percentage of the variance, hence carrying most of the vital information needed, while leaving out any other parameters that could have corrupted the signals, such as noise or temperature variation.

4.3. Lock-in thermography

During testing of the vertical stabilizer, lock-in images were recorded. Both amplitude and phase images were acquired. Amplitude images present the temperature-difference acquired on a pixel by-pixel-basis whereas phase delay images are time-dependent showing the thermal wave decay in time [40]. A close-up of the recorded area is shown in Fig. 16 which also depicts a

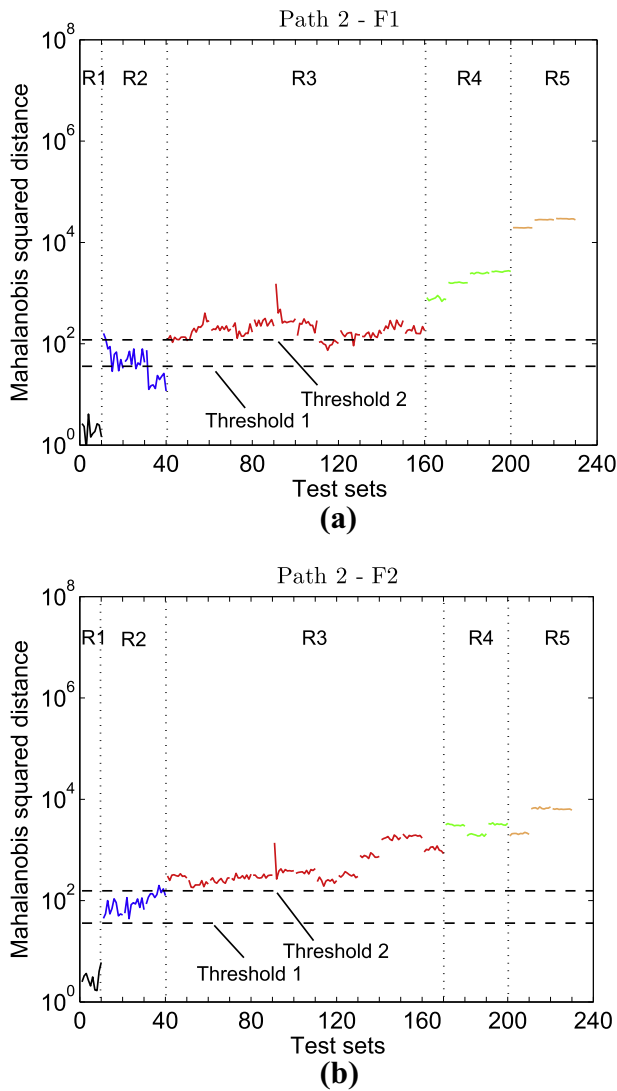


Fig. 15. (a) Outlier analysis at the first 10 principal components for path 2, corresponding to feature 1 (F1) and (b) feature 2 (F2).

representative thermographic image acquired at the initiative fatigue cycles.

Dynamic testing of the aluminium structure was performed until substantial critical failure of the patch (i.e. its detachment

from the parent structure), as was indicated by the on-line thermographic inspection. The real time evaluation of the phase and amplitude images indicated that after approximately 600 kcycles, the CFRP patch was almost fully detached from the aluminium substrate. Only one small area exhibited some bonding with the substrate. As was decided, the test was stopped before the complete separation of the patch from the parent surface took place. In this way, a cross-validation with ultrasonics (C-scan) would be feasible to benchmark the efficiency of thermography.

Phase and amplitude images at specific loading cycles are presented in Figs. 16 and 17 illustrating the whole deterioration evolution of the patch/substrate interface.

Starting with the first lock-in amplitude image in Fig. 16(b), the applied bonded patch is clearly identified. As may be observed next to the bonded patch, the piezoelectric sensors for Lamb wave monitoring may be discerned. The rivet/bolted joint thermal imprint is also clearly visible. Moreover, a relatively small high amplitude or stress concentration area around the rivet was acquired. The rest of the patched area does not exhibit any significant variations, suggesting a uniform temperature and stress distribution all over the bonded zone. At this stage, the artificially induced crack is not discernible, suggesting that the patch eliminates locally induced stress concentrations. At 50 kcycles, the phase and amplitude gradients become significant and in both lock-in (magnitude and phase) images (Fig. 17(a)) the crack was visible. In the phase image, the full length of the crack can be seen. This is not the case for the amplitude image, probably because the surface topology inhibits the observation of internal defects. As the load level increased, stress concentrations around the rivet became more pronounced. The relative phase and amplitude gradients increased, suggesting a substantial increase of the stress concentration in the region surrounding the rivet. At 330 kcycles (Fig. 17(b)) a dark region was detected in the amplitude image. The same region was clearly presented with bright colour by the phase one. With the increase in load level and fatigue progression this behaviour became more prominent with the enlargement of the dark region shown in the amplitude imprint as well as its gradual shifting towards the horizontal axis of the image (Fig. 17(c)). At 430 kcycles (Fig. 17(d)) the dark region on the amplitude image reached the right edge of the patch. This is verified by the phase image (430 kcycles), which shows an extended bright area which propagates to the tapered right edge of the patch.

This gradual radial propagation of stress concentration areas with the same profile was noted, as fatigue loading continued. At 480 kcycles (Fig. 17(e)), the area with increased stress concentration caused by the bolted joint, reached the left (as indicated on the image) edge of the patch. The same behaviour consistently

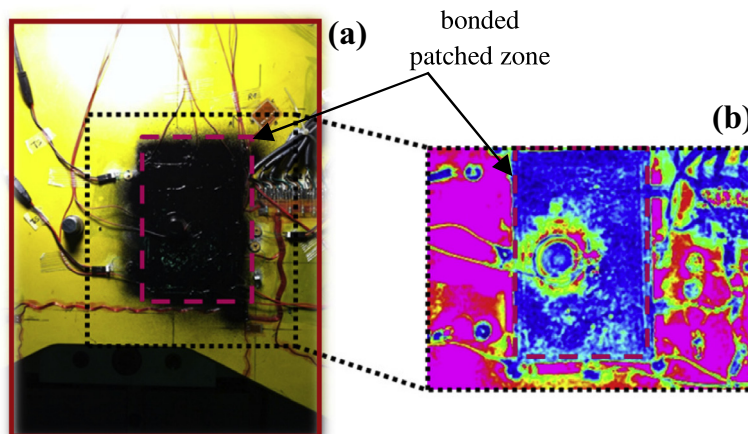


Fig. 16. (a) Monitored area, (b) representative thermographic image.

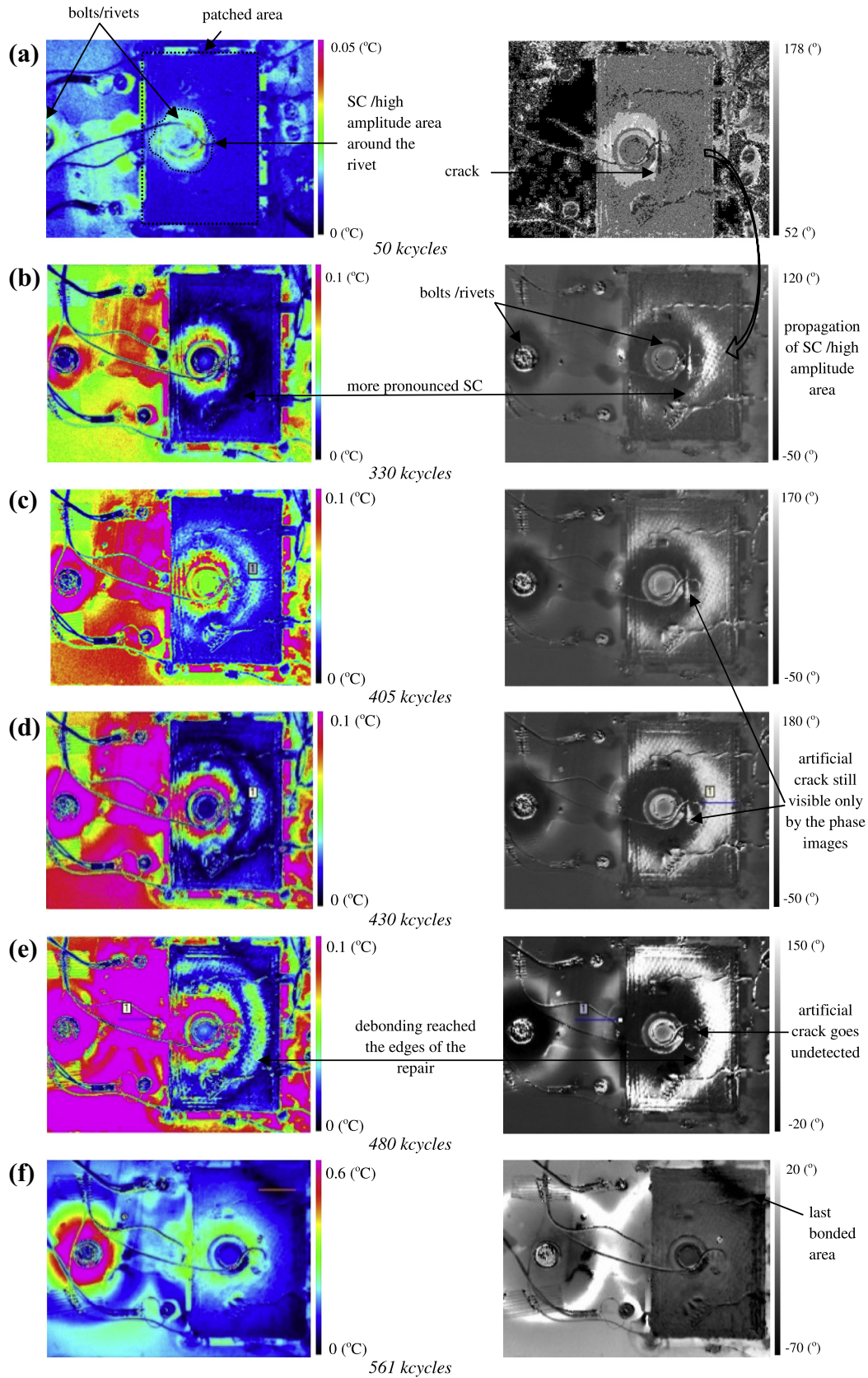


Fig. 17. Amplitude (left-hand side) and phase (right-hand side) images.

continued up to the final loading step of the fatigue testing (Fig. 17(f)) at 561 kcycles. At the acquired last lock-in images (Fig. 17(f)), only a small dark region is presented on the right upper

corner of the patch. This was considered as the last bonded area of the patch. For this reason, it was decided to stop the test process and verify this observation with c-scanning of the patched area.

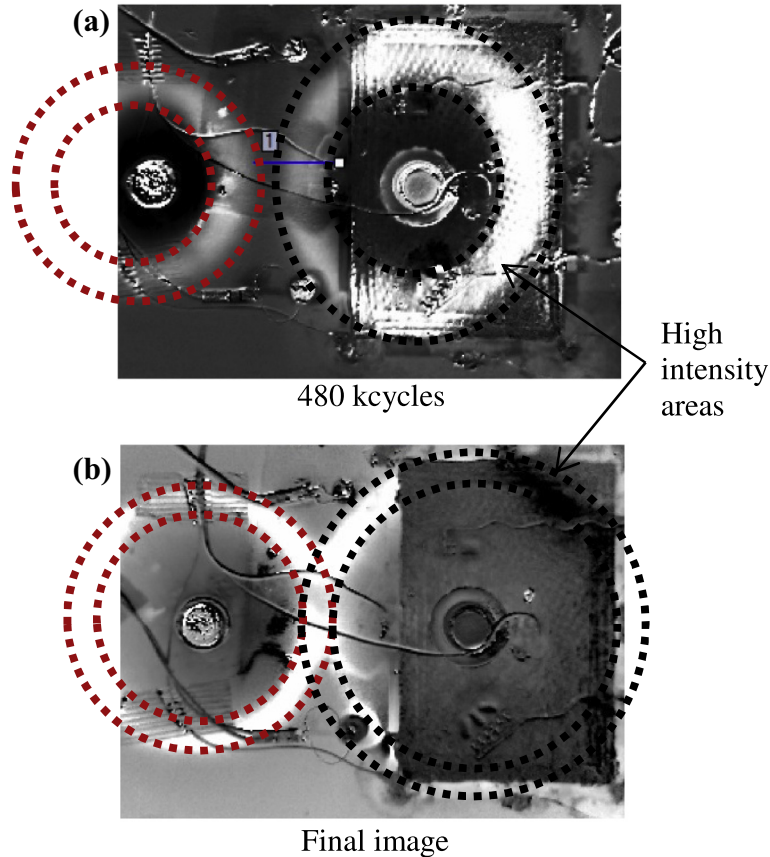


Fig. 18. Lock-in phase images at (a) 480 kcycles and (b) 561 kcycles (final stage).

The verification with ultrasonic imaging would assure the effectiveness of the thermographic method on monitoring damage initiation and propagation during service.

A closer examination of the whole lock-in image sequence denotes that besides stress concentration around the patched rivet, circularly-shaped high intensity areas were recorded around the patch-free rivet. It is noteworthy, that as the last recorded lock-in images indicate, the mechanical stresses/high amplitude areas have diminished from the patched rivet. This observation suggests the following (and probably complementary effects): (i) complete stress relaxation on the patched area and (ii) complete failure of the patch/substrate interface. The latter inhibits the visibility of high amplitude areas/stress concentrations around bolted joint which are clearly identified around the un-patched rivet area (Fig. 17(f)).

Fig. 18(a) and (b) depict a comparative evaluation between a lock-in image at 480 kcycles and the one acquired at the final

stage. The stress concentrations around the bolted joints of Fig. 18(a) form patterns possessing a radial symmetry. These circular patterns indicate high amplitude areas/stress concentrations both in the unrepaired and the repaired rivet sites. Mechanically-induced stresses around the patched joint can be distinguished, due to the fact that the patch remains bonded on the substrate. However, this is not the case in the final recorded image (Fig. 18(b)). After the almost complete separation of the patch, the suggested high amplitude/stress concentration areas were not detected on the patched zone. To further elucidate the above statements, circles showing the presence (or absence) of stress concentration areas around the bolted joints were drawn (Fig. 18(a) and (b)). The centres of the drawn circles correspond to the position of the rivets (unpatched-left side and patched-right side).

Moreover, the juxtaposition of images in Fig. 18 denotes that the diameters of the figurative high amplitude/stress concentration

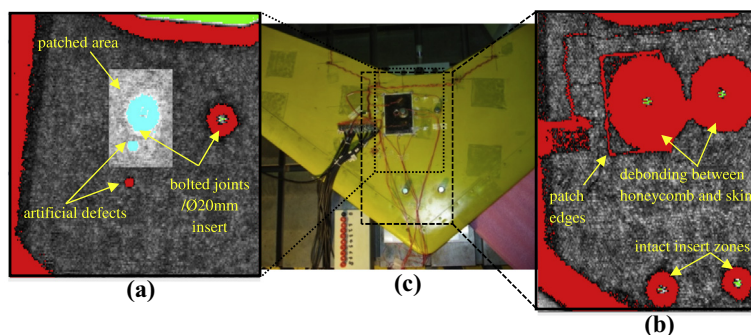


Fig. 19. Ultrasonic images of the stabilizer (a) prior and (b) post testing, (c) repaired wing stabilizer.

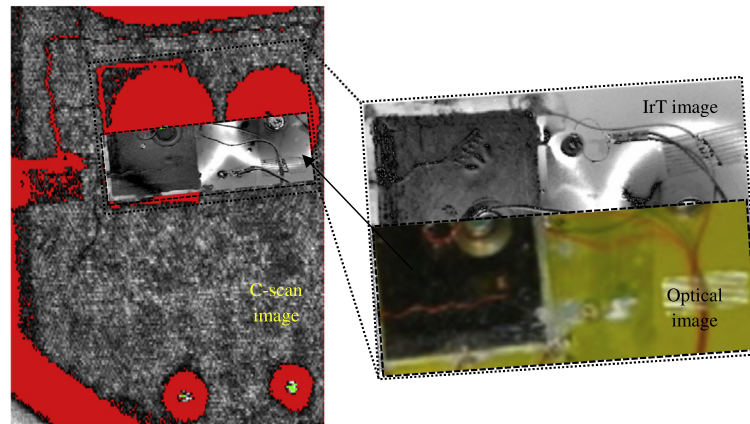


Fig. 20. Overlapping of ultrasonic, optical and thermographic images.¹

circles around the rivets have increased. This suggests that apart from the degradation of the patch/substrate interface, a second deterioration mechanism may be present; as the interrogated vertical stabilizer is a sandwich structure, it is highly probable that the local stress concentration also invoked the failure of the interface between the honeycomb and the aluminium skin. Ultrasonic imaging verified this hypothesis.

4.4. Ultrasonic testing (C-scan)

As is shown in Fig. 19(a) where the C-scan of the repaired stabilizer prior to testing is shown, the rectangle-shaped CFRP patch can be seen upon the $\varnothing 20$ mm insert. The patched and unpatched cylindrical insert, where the rivets are fixed are well discerned and, in addition, two artificially induced flaws (simulating manufacturing defects) were also visible. On the contrary, in the post-testing C-scan imaging, the patch goes totally undetected. Only the edges of the patch can be seen, at the very same external areas where sealant tape was placed to prevent from water penetration after immersion in the C-scan tank.

Together with the edges of the patch, the debonded honeycomb/skin interface is well verified with ultrasonics. Fatigue mechanical testing led to the detachment of the internal core of the stabilizer from the aluminium skin, at the very same areas where the cylindrical inserts of the rivet/bolted joints are located. Fig. 20 shows an overlapping of an optical, the final phase and the post-testing C-scan image. The areas around the inserts/rivets which exhibited high amplitude areas/stress concentrations can be identified and correlated both via the ultrasonic and thermal imaging. It is also worth mentioning that the area in the vicinity of the other two bolted joints remained intact after the test procedure (discernible in the C-scan image and Fig. 19(b)).

5. Conclusions

An aluminium helicopter tail stabilizer with an artificially introduced through-thickness crack was tested under bending fatigue. The crack was repaired with a one-sided composite patch cured with a heating blanket. The structural performance was continuously monitored with both Lamb waves and lock-in thermography while the assessment of the final stage damage was performed with ultrasonic C-scan testing. Four piezoelectric transducers were surface-bonded on the aluminium stabilizer at appropriate locations close to the patch, forming two propagation paths covering the most critical areas of the repaired region. Appropriate features were selected which enabled the characterisation of different parts of the signals. Outlier and principal component analysis were

conducted in order to identify the number of cycles where damage started developing in the form of patch debonding and honeycomb detachment from the skin. For the lock-in thermography, an infrared camera was placed in the required distance in order to provide the necessary field of view above the repaired surface of the stabilizer. Amplitude and phase images were acquired during mechanical testing depicting the evolution of the structural deterioration of the bonded repair. Both methods proved damage sensitive, enabling a continuous characterisation of the integrity of the monitored system.

For the outlier analysis with Lamb waves, the assignment of a second threshold apart from the Monte Carlo was performed, in order to account for the irregularities introduced to a number of factors that could affect the obtained data at early normal or near-normal condition stages and potentially lead to false alarms. The modified outlier analysis enabled the isolation of five regions which were further correlated with the damage accumulation during fatigue, in significant agreement with results obtained from lock-in thermography. Principal component analysis enabled the separation of the clusters which were further attributed to the different stages of damage accumulation around the rivets showing that it gradually propagated and reached the edges of the patch. The principal curves were further fitted on the PCA clusters which could provide a further tool aiming at the reduction of the dimensions of a complex monitored system, a method which needs further refinement. Finally the reduction of the dimensions prior to the outlier analysis was possible through the isolation of appropriate principal components which account for the highest percentage of variance. These then were selected as features on which outlier analysis was performed. Results indicated that the performance of the outliers was slightly improved in contrast to the application of outlier analysis on features selected directly from the recorded time signals.

From the onset of the experiment, high amplitude/stress concentrations were recorded around both patched and un-patched rivets/bolted joints from the lock-in thermography. A radial progress of the high intensity circular area was observed in both amplitude and phase images which became more pronounced as fatigue testing continued. This area gradually reached all edges of the applied patch indicating the complete patch debonding. At the final recorded lock-in images, the figurative stress concentration ring had totally vanished from the patch zone, verifying the above postulation. Comparing the high intensity rings formed around the patched and un-patched rivets, showed that stresses, which were identically distributed during testing, are no longer visible on the patched zone. This was attributed to the patch/skin interface failure. Along with the patch/substrate interface

deterioration, thermography detected a secondary deformation mechanism of the stabilizer; the honeycomb – skin interface failure.

C-scanning inspection, prior to and after testing, verified this hypothesis. The post-failure ultrasonic image could not identify the patch, albeit it showed an extensive debonding between the skin and the underlying honeycomb core of the sandwich structure. The combined image where thermographic, ultrasonic and optical photographs are juxtaposed is also indicative of the honeycomb core/skin interlaminar failure, Fig. 20. Finally, post-failure optical images show the disruption of the film in most patch edges, except for those around the small remaining bonded areas as was observed via the evaluation of the thermographic images, Fig. 8.

The work highlighted the capability of the two methods for the monitoring of the structural integrity and repair efficiency in aircraft structures in a comparable and complimentary way, exhibiting good agreement. They can be both employed to provide qualitative and quantitative information even in full scale aircraft structural components in relation to the efficiency of the applied repair methodology with a view to its qualification, certification and endorsement by the aircraft industry.

Acknowledgements

The authors would like to acknowledge the financial support from the EU 7th Framework Programme IAPETUS (innovative repair of aerospace structures with curing optimisation and life cycle monitoring abilities).

References

- [1] Avram JB. Fatigue response of thin stiffened aluminium cracked panels repaired with bonded composite patches. Tech. rep., DTIC Document; 2001.
- [2] Baker AA, Rose LF, Jones R. *Advances in the Bonded Composite Repair of Metallic Aircraft Structure*, 1. Elsevier Science; 2003.
- [3] Papanikos P, Tserpes K, Labeas G, Pantelakis S. Progressive damage modelling of bonded composite repairs. *Theoret Appl Fract Mech* 2005;43(2):189–98.
- [4] Hart-Smith L. Further developments in the design and analysis of adhesive-bonded structural joints. *Joining Compos Mater BASTM STP* 1981;749:3–31.
- [5] Hart-Smith L. An engineer's viewpoint on design and analysis of aircraft structural joints. *Proc Inst Mech Eng Part G* 1995;209(G2):105–29.
- [6] Hu F, Soutis C. Strength prediction of patch-repaired CFRP laminates loaded in compression. *Compos Sci Tech* 2000;60(7):1103–14.
- [7] Albedah A, Bouiadra BB, Mhamdia R, Benyahia F, Es-Saheb M. Comparison between double and single sided bonded composite repair with circular shape. *Mater Des* 2011;32(2):996–1000.
- [8] Soutis C, Hu FZ. Design and performance of bonded patch repairs of composite structures. *Proc Inst Mech Eng Part G J Aeronaut Eng* 1997;211(4):263–71.
- [9] Umamaheswar TV, Singh R. Modelling of a patch repair to a thin cracked sheet. *Eng Fract Mech* 1999;62(23):267–89.
- [10] Ouinas D, Bouiadra B, Serier B, SaidBekkouche M. Comparison of the effectiveness of boron/epoxy and graphite/epoxy patches for repaired cracks emanating from a semicircular notch edge. *Compos Struct* 2007;80(4):514–22.
- [11] Hosseini-Toudeshky H, Mohammadi B. Thermal residual stresses effects on fatigue crack growth of repaired panels bounded with various composite materials. *Compos Struct* 2009;89(2):216–23.
- [12] Hosseini S, Duczek S, Gabbert U. Damage localization in plates using mode conversion characteristics of ultrasonic guided waves. *J Nondestr Eval* 2014;33(1):152–65.
- [13] Baker A. Bonded composite repair of fatigue-cracked primary aircraft structure. *Compos Struct* 1999;47(1–4):431–43.
- [14] Grammatikos S. Structural integrity assessment of aerostructures using innovative Non-Destructive Techniques [Ph.D. thesis], Materials Science & Eng. Dept., University of Ioannina; 2013.
- [15] Caminero M, Pavlopoulou S, Lopez-Pedrosa M, Nicolaisson B, Pinna C, Soutis C. Analysis of adhesively bonded repairs in composites: damage detection and prognosis. *Compos Struct* 2013;95:500–17.
- [16] Farrar C, Worden K. An introduction to structural health monitoring. *Philos Trans R Soc A Math Phys Eng Sci* 2007;365(1851):303–15.
- [17] Jones R, Galea S. Health monitoring of composite repairs and joints using optical fibres. *Compos Struct* 2002;58(3):397–403.
- [18] Qing XP, Beard SJ, Kumar A, Hannum R. A real-time active smart patch system for monitoring the integrity of bonded repair on an aircraft structure. *Smart Mater Struct* 2006;15(3):N66.
- [19] Rose J. *Ultrasonic waves in solid media*, vol. 10. Cambridge University Press; 1999.
- [20] Giurgiutiu V. *Structural health monitoring: with piezoelectric wafer active sensors*. Academic Press; 2007.
- [21] Kessler SS, Spearing SM, Soutis C. Damage detection in composite materials using Lamb wave methods. *Smart Mater Struct* 2002;11(2):269.
- [22] Worden W, Pierce SG, Manson G, Philp WR, Staszewski WJ, Culshaw B. Detection of defects in composite plates using lamb waves and novelty detection. *Int J Syst Sci* 2000;31(11):1397–409.
- [23] Diamanti K, Soutis C, Hodgkinson J. Non-destructive inspection of sandwich and repaired composite laminated structures. *Compos Sci Tech* 2005;65(13):2059–67.
- [24] Soutis C, Ihn J. Design, analysis, and shm of bonded composite repair and substructure. *Encyclopedia of Structural Health Monitoring*.
- [25] Worden K, Manson G, Fielner NRJ. Damage detection using outlier analysis. *J Sound Vib* 2000;229(3):647–67.
- [26] Pavlopoulou S, Soutis C, Manson G. Non-destructive inspection of adhesively bonded patch repairs using Lamb waves. *Plast Rubber Compos* 2012;41(2):61–8.
- [27] Pavlopoulou S. On structural health monitoring of aircraft adhesively bonded repairs [Ph.D. thesis]. University of Sheffield; 2013.
- [28] Chetwynd D, Rongong JA, Pierce SG, Worden K. Damage detection in an aluminium plate using outlier analysis. *Fatigue Fract Eng Mater Struct* 2008;31(8):629–43.
- [29] Yan A, Kerschen G, Boe PD, Golinvall J. Structural damage diagnosis under varying environmental conditions. Part I: a linear analysis. *Mech Syst Signal Processing* 2005;19(4):847–64.
- [30] Hsu TY, Loh CH. Damage detection accommodating nonlinear environmental effects by nonlinear principal component analysis. *Struct Control Health Monit* 2010;17(3):338–54.
- [31] Worden K. Inferential parametrisation using principal curves. *Proceedings of 3rd international conference on identification of engineering systems*, Swansea, UK, 2002, p. 341–52.
- [32] Hastie T, Stuetzle W. Principal curves. *J Am Stat Assoc* 1989;84:502–16.
- [33] Grammatikos SA, Kordatos EZ, Matikas TE, Paipetis AS. Real-time debonding monitoring of composite repaired materials via electrical, acoustic, and thermographic methods. *J Mater Eng Perform* 2014;23:169–80.
- [34] Kordatos EZ, Aggelis DG, Matikas TE. Monitoring mechanical damage in structural materials using complimentary NDE techniques based on thermography and acoustic emission. *Compos Part B Eng* 2012;43:2676–86.
- [35] Kulkarni R, Ochoa O. Transverse and longitudinal CTE measurements of carbon fibers and their impact on interfacial residual stresses in composites. *J Compos Mater* 2006;40(8):733–54.
- [36] Rogers KF, Kingston-Lee DM, Phillips LN, Yates B, Chandra M, Parker S. The thermal expansion of carbon-fibre reinforced plastics. *J Mater Sci* 1981;16(10):2803–18.
- [37] Wong AK. A non-adiabatic thermoelastic theory for composite laminates. *J Phys Chem Solids* 1991;52(3):483–94.
- [38] Stanley P, Chan WK. Quantitative stress analysis by means of the thermoelastic effect. *J Strain Anal Eng Des* 1985;20(3):129–37.
- [39] Tarassenko L. *Guide to neural computing applications*. Hodder Arnold Publication, Elsevier Science; 1998.
- [40] Maldague X. Introduction to NDT by active infrared thermography. *Mater Eval* 2002;60(9):1060–73.